



Fabrication of inverse opal TiO₂-supported Au@CdS core-shell nanoparticles for efficient photocatalytic CO₂ conversion

Yuechang Wei¹, Jinqing Jiao¹, Zhen Zhao^{*}, Jian Liu^{**}, Jianmei Li, Guiyuan Jiang, Yajun Wang, Aijun Duan

State Key Laboratory of Heavy Oil Processing, China University of Petroleum, Beijing 102249, China

ARTICLE INFO

Article history:

Received 31 March 2015

Received in revised form 16 May 2015

Accepted 20 May 2015

Available online 23 May 2015

Keywords:

Inverse opal materials

TiO₂

Core-shell structure

Photocatalysis

CO₂ conversion

ABSTRACT

The photocatalytic conversion of CO₂ with H₂O into renewable hydrocarbon fuels by solar energy is of significance in solving both energy and environmental problems. Herein, we firstly report a practical fabrication of all-solid-state three-component Z-scheme system with the core-shell structured Au@CdS core-shell nanoparticles on inverse opal TiO₂ (Au@CdS/IO-TiO₂) via the gas bubbling-assisted membrane reduction-precipitation (GBMR/P) method. All the catalysts possess well-defined inverse opal structure with the interconnected networks of spherical voids, and the Au@CdS core-shell nanoparticles with different molar ratios of Cd/Au are well dispersed and supported on the inner wall of uniform macropore. The slow photon effect of inverse opal structure with moderate macropore sizes can enhance the light-harvesting efficiency. And the all-solid-state Z-scheme system with CdS(shell)-Au(core)-TiO₂(support) nanojunction is favourable for the separation of photogenerated electrons and holes due to the vectorial electron transfer of TiO₂ → Au → CdS. The Au@CdS/IO-TiO₂ catalysts exhibit super photocatalytic performance for CO₂ reduction to CH₄ under the simulated solar irradiation. Among the as-prepared catalysts, Au@CdS/IO-TiO₂-1 catalyst with the moderate thickness of CdS nanolayer shell shows the highest photocatalytic activity and selectivity for CO₂ reduction, e.g., its formation rate of CH₄ is 41.6 μmol g⁻¹ h⁻¹ and its selectivity to CH₄ production by CO₂ reduction is 98.6%. The design and versatile synthetic approach of all-solid-state Z-scheme system on the surface of inverse opal oxides are expected to throw new light on the fabrication of highly efficient photocatalyst for CO₂ reduction to hydrocarbon.

Crown Copyright © 2015 Published by Elsevier B.V. All rights reserved.

1. Introduction

In recent years, solar photocatalytic conversion of CO₂ with H₂O to hydrocarbon fuels has sparked a new sustainable development path, since it would help to reduce atmospheric CO₂ level and partly fulfill energy demands [1]. The conversion of CO₂ with H₂O, two very stable molecules accompanied with a large positive change in the Gibbs free energy, is one of the biggest challenges in chemistry [2]. The solar photocatalytic conversion of CO₂ and H₂O to produce fuels and chemicals can be realized by using active photocatalysts. Since the pioneering studies by Inoue and Fujishima et al. [3], many studies have been devoted to the design and synthesis of efficient photocatalysts for the CO₂ reduction [4–7]. In

this heterogeneous process, the photocatalyst is usually a hybrid semiconductor material which can absorb light, separate the photogenerated electron-hole pairs, transport them to the surface and provide active sites for the catalytic reaction [8,9]. Among the various photocatalysts, titanium dioxide (TiO₂) is the most common and promising photocatalyst for solar-fuel production owing to its cheapness, availability, photostability and nontoxicity [10–13]. However, the photocatalytic activity of pure TiO₂ under visible light irradiation is not high enough for practical application due to the drawbacks of the wide band gap, the low absorption efficiency of solar irradiation and the easy charge recombination [14]. Therefore, the improving activity of TiO₂-based photocatalysts mainly involves increasing light absorption, photogenerated charge transfer/separation, and the subsequent catalysis, etc.

Recently, the unique optical performance of inverse opal (IO) or three-dimensionally ordered macroporous (3DOM) materials as a kind of photonic crystal for light harvesting via slow photon enhancement has been attracting strong interest in photocatalysis and photoelectrochemistry [15–17]. IO or 3DOM structures have been reported to enhance the light absorption of a material and

^{*} Corresponding author at: 18# Fuxue Road, Chang Ping District, Beijing 102249, China. Tel.: +86 10 89731586; fax: +86 10 69724721.

^{**} Corresponding author.

E-mail addresses: zhenzhao@cup.edu.cn (Z. Zhao), liujian@cup.edu.cn (J. Liu).

¹ These authors contributed equally to this work.

improve its photoreaction efficiency as well [18]. Slow photons of IO structures, known as photonic crystals, are capable of achieving this goal. Photonic crystals have periodic modulations of the refractive index on the length scale of the light wavelength, thus forbidding certain wavelengths of light to propagate through the materials and resulting in a stop-band reflection because of coherent Bragg diffraction [19]. The stop-band reflection frequencies depend on the periodicity and dielectric contrast of the photonic crystal. Slow photons effect appearing in photonic structures could increase the path length of the light, as the group velocity of light at the edge of these wavelengths decreases dramatically. For applications in photocatalysis, it is expected that overlap of the energy of slow photons and the absorbance of the material will enhance the materials' light absorption. This possible enhancement opens an alternative and attractive route to increase the photocatalytic efficiency when the corresponding photonic stop-band edge matches the irradiation wavelength [20].

In addition, many strategies have been developed to improve photocatalytic efficiency via the second-component doping to promote the photogenerated charge separation, harvesting visible light and facilitating CO₂ activation [21–25]. Among these tactics, constructing TiO₂-based heterostructure has been demonstrated effective for improving photocatalytic efficiency through promoting the photogenerated charge separation, harvesting visible light and facilitating CO₂ activation [26,27]. Various types of second-component semiconductor of TiO₂-based heterostructure have been reported, such as CdS [28], CeO₂ [29] and ZrO₂ [30] and so on. On this basis, an electron transfer mediator (Pt [31], Au [32], and graphene oxide [33–35]) embed in the heterostructure interface can strengthen the interface charge transfer and result in a vectorial electron transfer via a Z-scheme system [36], which can efficiently improve photogenerated electron-hole pair separation and photocatalytic activity. For all the above prominent advantages, the construction of three-component heterostructure combined with inverse opal structure is expected to bring high performance and powerful platforms for photocatalytic CO₂ reduction.

Herein, we firstly report a practical fabrication of visible light responsive all-solid-state three-component Z-scheme system with the core-shell structured Au@CdS nanoparticles (NPs) on inverse opal TiO₂ (Au@CdS/IO-TiO₂) via the gas bubbling-assisted membrane reduction-precipitation (GBMR/P) method. Our design and versatile synthetic approach can control the macropore sizes of inverse opal oxides via the microsphere sizes of colloidal crystal template and the nanolayer thickness of the CdS shell over Au core NPs at the nanoscale via the adjustable molar ratio of Cd/Au. The slow photon effect of inverse opal structure with suitable pore size can enhance the light-harvesting efficiency. And the all-solid-state Z-scheme system with CdS(shell)-Au(core)-TiO₂(support) nanojunction is favorable for improving the separation of photogenerated electrons and holes. This three-component system exhibits high photocatalytic activity for CO₂ reduction to CH₄ under the simulated solar irradiation, far exceeding those of the single- and two-component systems. It suggests that Au@CdS/IO-TiO₂ catalysts are excellent system for photocatalytic reactions or surface chemical processes that occur at the interfaces of reactant and catalyst.

2. Experimental

2.1. Preparation of materials

2.1.1. Synthesis of inverse opal TiO₂-supported Au@CdS core-shell NP catalysts

Synthesis of monodispersed polymethyl methacrylate (PMMA) microsphere, assembly of template, and IO-TiO₂ support by

colloidal crystal template (CCT) method is similar to that described previously [37,38]. The IO-TiO₂ support was obtained via calcination at 600 °C for 5 h. The Au@CdS/IO-TiO₂ catalysts were synthesized by two-step process of the gas bubbling-assisted membrane reduction-precipitation (GBMR/P) method. The typical preparative procedures were described as follows: First step is the preparation of IO-TiO₂-supported Au NPs via GBMR method [39]. Second step is the preparation of CdS NP coated on the surface of Au/IO-TiO₂ catalyst using GBMP method [40]. The final products were calcined in an oven at 100 °C for 2 h and the desired Au@CdS/IO-TiO₂ catalysts were obtained.

2.2. Characterization

The nitrogen adsorption/desorption isotherm measurement were carried out at −196 °C by using an automated gas sorption analyzer (Quantachrome Autosorb-iQ, USA) after having degassed the sample for 4 h at 300 °C. The specific area was calculated from the Brunauer–Emmett–Teller (BET) equation using P/P^0 values between 0.05 and 0.3. Mercury intrusion porosimetry experiments were carried out on a Micromeritics AutoPore IV 9500 apparatus in the pressure range 0–30000 psia. XRD patterns were measured on a powder X-ray diffractometer (Shimadzu XRD 6000) using Cu K α ($\lambda = 0.15406$ nm) radiation with a Nickel filter operating at 40 kV and 10 mA in the 2θ range of 15–90°. The UV–vis DRS experiments were performed on a UV–vis spectrophotometer (Hitachi U-4100) with the integration sphere diffuse reflectance attachment. The surface morphology of the samples was observed by SEM (FEI Quanta 200F). The TEM and HRTEM images were carried out using a JEOL JEM 2100 electron microscope equipped with a field emission source at an accelerating voltage of 200 kV. The average particle diameter was calculated from the mean diameter frequency distribution with the formula: $d = \sum n_i d_i / \sum n_i$, where n_i is the number of particles with particle diameter d_i in a certain range. The actual content of Au in catalysts was determined by inductive coupled plasma atomic emission spectrometry (ICP-AES) (PE, OPTIMA 5300DV). X-ray photoelectron spectra (XPS) were recorded on a PerkinElmer PHI-1600 ESCA spectrometer using Mg K α ($h\nu = 1253.6$ eV, $1 \text{ eV} = 1.603 \times 10^{-19}$ J) X-ray source. The binding energies were calibrated using C1s peak of contaminant carbon (BE = 284.38 eV) as an internal standard. The photoluminescence (PL) spectra of the as-prepared samples were measured using a Hitachi F-4600 fluorescence spectrophotometer. The solid catalysts are placed in the standard slot and are compacted by the quartz glass. The semiconductor material is first irradiated by the excitation light and absorbs the photon energy, and then the electron-hole pairs are produced in the semiconductor material. Finally, the recombination of electron-hole pairs on the surface of semiconductor can produce the PL emission spectra. The working electrode of photocurrent measurement was made by transferring the catalysts into film electrode. The working electrode was obtained by dip-coating catalyst slurry (5 mg/ml in ethanol) onto indium-tin oxide (ITO) glasses. Then slurry (0.020 ml) was spreading onto ITO glass with an exposed area of 0.25 cm². After dried in the air for 24 h, a copper wire was connected to the side part of the ITO glass using conductive tape. Photocurrent measurements were carried out on a CHI Electrochemical System in the mixture of MeCN and H₂O ($v/v = 3/2$) without any bias potential at room temperature. A graphite rod and an Ag/AgCl (3 M KCl) electrode were used as the counter electrode and reference electrode, respectively. During the measurements, to minimize the influence of the semiconductor layer, the working electrodes were irradiated from the back side.

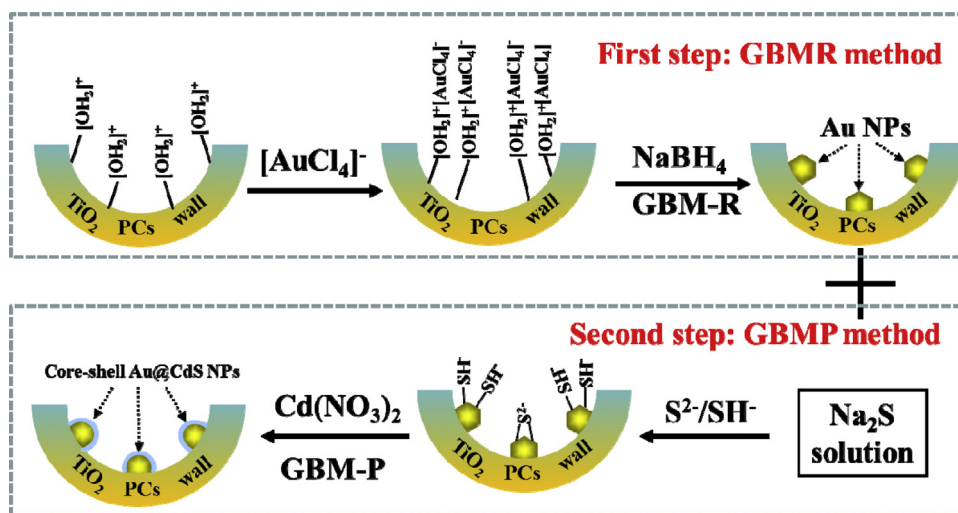


Fig. 1. Schematic for the two step synthesis of Au@CdS core-shell NPs supported on the surface of inverse opal TiO₂ carrier by the GBMR/P method.

2.3. Catalytic activity measurements

The photocatalytic reduction of CO₂ with H₂O was carried out in a gas-closed circulation system, 0.02 g of the tested catalyst was put in a glass reactor with a basal diameter of 6.5 cm by spin-coating. The light source was a 300 W Xe lamp ($\lambda = 320\text{--}780\text{ nm}$) using the simulated sunlight purchased from Perfect Light Co. The intensity of incident light at the location of catalyst was measured to be 100 mW cm^{-2} by a spectroradiometer. The reaction device was vacuum-treated several times, and then the high purity of CO₂ gas was flowed into the reaction setup for reaching ambient pressure. Compressed CO₂ (99.999%) was passed through a deionized water bubbler to introduce CO₂ and water vapor mixture into the photoreactor. The pressure of CO₂ was regulated to 0.1 MPa. Before irradiation, the as-prepared photocatalysts were kept in the CO₂-H₂O atmosphere for several hours to ensure the absorption of gas molecules for equilibrium. The photocatalytic reduction of CO₂ with H₂O was typically carried out at 298 K for 2 h in each run. The products were analyzed by using an on-line gas chromatograph (GC-9560; HuaAiSePu Corp., China) equipped with a thermal conductivity detector (TCD) with 5A column for product analyses of H₂ and O₂ and a flame ionization detector (FID) with TDX-01 column for product analysis of CO and CH₄. The quantification of the products was based on the external standard with the use of a calibration curve. The catalytic activity was evaluated by the formation rates of H₂, CO and CH₄, selectivities for CO₂ reduction, CO and CH₄ production for photocatalytic conversion of CO₂ with H₂O.

3. Results

3.1. Synthesis mechanism of 3DOM Pt@CdS/TiO₂ catalysts via the GBMR/P method

The effective control of the dispersion and structure of supported metal@sulfide core-shell NPs on the surface of 3DOM oxides is a primary goal of catalyst design and is quite challenging. It is well-known that the nucleation and growth of metal or sulfide nanocrystal govern the particle size and morphology in the synthesis process by precipitation or reduction [41,42]. Fig. 1 shows the synthesis schematic of two-step GBMR/P method for Au@CdS/IO-TiO₂ catalysts. The highly homogeneous dispersion of reductant/precipitant may be an operative means to regulate the nucleation process so as to produce a mass of Au or CdS nucleus [43]. The GBMR/P method can be divided into two steps: GBMR and GBM-P processes. For the GBMR processes, [AuCl₄]⁻ ions

are adsorbed and anchored on surface [OH₂]⁺ groups of the IO-TiO₂, because the pH value of mixture solution (~ 3.0) using the adjustment of HCl solution is far lower than the isoelectric point (IEP) of the TiO₂ support. When NaBH₄ solution was injected into the tubular reactor through the holes of ceramic membrane tubes, the reduction of [AuCl₄]⁻ occurred immediately to give Au nucleus (nucleation) with the convenient protection (PVP) on the surface of IO-TiO₂. Therefore, the uniform distribution size of Au NPs on IO-TiO₂ can be obtained. For GBMP process, it can efficiently disperse the CdS NPs on the surface of Au NPs. Before the Cd(NO₃)₂ solution was involved, S²⁻ or [HS]⁻ ions derived from the hydrolysis of Na₂S are adsorbed and anchored on surface of supported Au NPs [44]. When the Cd(NO₃)₂ solution was injected into the tubular reactor through the holes of ceramic membrane tubes, the precipitation between Cd²⁺ and S²⁻ occurred immediately to give CdS coated on the surface of supported Au NPs. The flow rate of the Cd(NO₃)₂ solution by a constant flow pump can control the deposition rate of CdS, and the molar ratio of Cd/Au can adjust the thickness of CdS nanolayer shell. Finally, the dispersion and morphology of supported Au@CdS core-shell NPs on the surface of IO-TiO₂ can be effectively controlled by the GBMR/P method.

3.2. The structure and optical property of IO-TiO₂

It is well-known that the photonic band gap of IO-TiO₂ materials can be regulated by the macropore sizes. In order to get appropriate photonic band gap to enhance the light harvesting efficiency via slow photon enhancement, we have synthesized a series of IO-TiO₂ materials with different pore sizes, and the results are shown in Fig. 2. Fig. 2(A–C) shows SEM image of the three-dimensional ordered PMMA colloidal crystal template with different average diameters obtained by centrifugation at 3000 r min^{-1} for 10 h. The average sizes of PMMA microspheres were determined to be 200, 250 and 360 nm, respectively. The colloidal crystals are self-assembled from monodisperse PMMA microspheres to a face-centered close-packed or opal arrangement. A liquid precursor of titania penetrates the opal and fills the voids of the templates. After solidification of the precursor, the colloidal templates are removed by calcination, yielding an inverse opal replica of the array of ordered spheres. The resulting solid skeleton is surrounded by air holes originating from the PMMA microspheres prior to removal. Where the original PMMA microspheres made contact, the macropores are interconnected by windows. As shown in Fig. 2(D–F), the porous structure of IO-TiO₂ is three-dimensionally highly ordered and contains a face-centred cubic (fcc) array. The

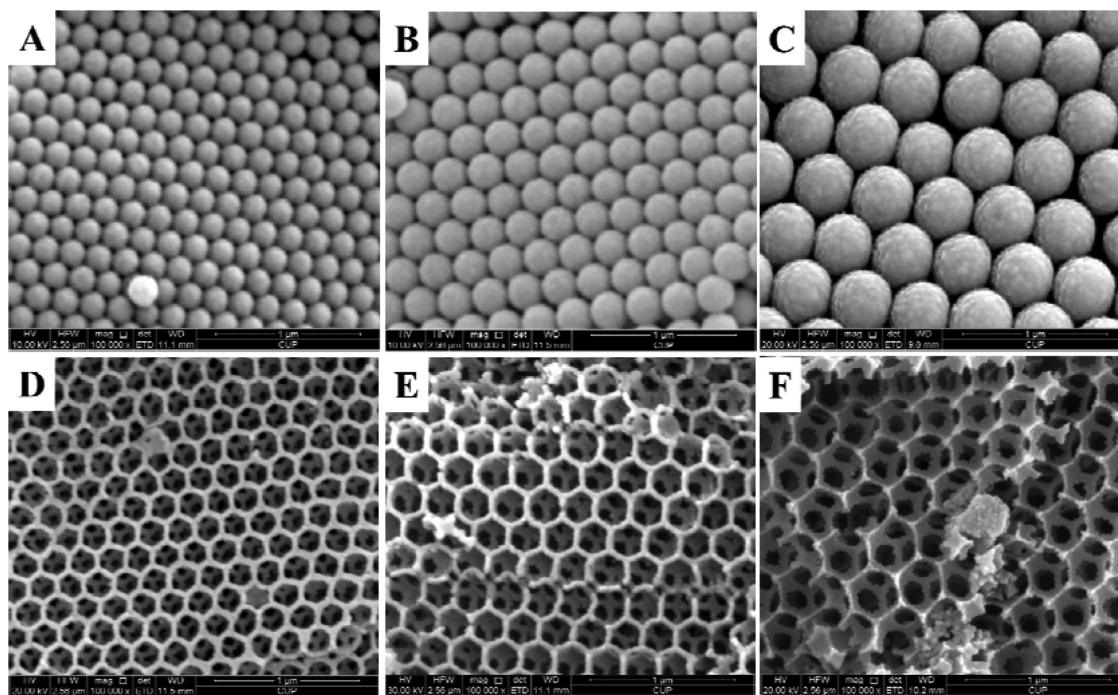


Fig. 2. SEM image of the three-dimensional ordered PMMA colloidal crystal template with different average diameters (A. 200 nm; B. 250 nm; C. 360 nm) and IO-TiO₂ catalysts with different pore sizes (D: 155 nm; E: 195 nm; F: 285 nm).

average pore diameters are about 155 nm, 195 nm and 285 nm, which are denoted as IO-TiO₂-155, IO-TiO₂-195 and IO-TiO₂-285, respectively. They correspond to shrinkage of 20–30% compared with the initial size (420 nm) of PMMA microspheres. The next layer is highly visible in SEM image and the voids are interconnected through open window. In addition, the wall thickness of IO-TiO₂ decreases with increasing of pore size. Different sizes and shapes of these interconnected macropores and different pore wall thicknesses alter the photonic band gap and change the light-scattering properties. Therefore, the diameters of PMMA microspheres can potentially tune the final photonic band gap.

The sizes of open windows were further assessed by means of mercury intrusion porosimetry (MIP) in Fig. 3. The diameter corresponding to the peak value of different curve is regarded as the most probable pore diameter, whose size occupies the largest proportion of pores compared with other pore diameters. It can be seen that the macropores (those in the 50–300 nm range) in this sample are very regular, and the most probable pore diameter are 55,

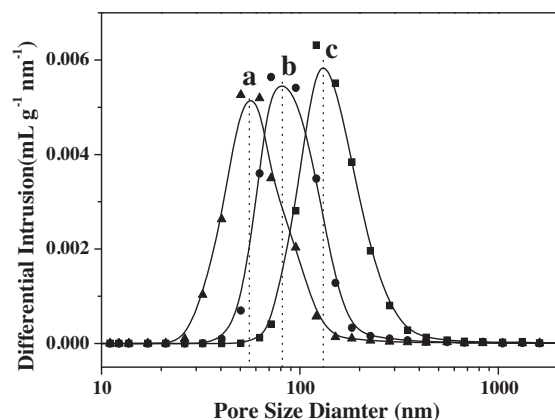


Fig. 3. The pore size distribution of IO-TiO₂ catalysts with different pore sizes determined by MIP. (a) IO-TiO₂-155; (b) IO-TiO₂-195; (c) IO-TiO₂-285.

80 and 120 nm, which is consistent with the size of open window observed in SEM images. The porosities, average pore diameters, total pore volumes and pore areas of IO-TiO₂ catalysts with different pore sizes were analyzed and compared, and the results are shown in Table 1. The total pore volume of IO-TiO₂ support determined by N₂ physisorption (<0.13 ml g⁻¹) is less than 10% of that (>1.4 ml g⁻¹) determined by MIP, indicating main contribution of macropores to the total porosity in these materials. Their average pore diameters of IO-TiO₂ catalysts obtained by different pore sizes of PMMA microspheres are 153, 191 and 274 nm, which is similar to the results of SEM images. And their porosities (>80%) are beyond 74% which is theoretical value of sphere volume in FCC array due to the shrinkage of oxide framework in the process of calcination.

Three dimensional photonic crystals can block light in a certain wavelength range, allowing the confinement and manipulation of photons in the materials. Fig. 4 shows the absorbance spectrum of crushed TiO₂ (left) and the reflectance spectra of as-prepared inverse opal PCs along the (1 1 1) plane after moistening by water (right). The photonic stop-band positions varied with the changing in the pore sizes, and red-shifted owing to larger pores packed with larger lattice constants. These strong Bragg reflection peaks indicate that it formed high-quality inverse opal structure in a long range. The IO-TiO₂-155, IO-TiO₂-195 and IO-TiO₂-285 materials show photonic stop-band position centered at 310, 372 and

Table 1

Porosities, average diameters, pore volumes and pore areas of IO-TiO₂ catalysts with different pore sizes.

Catalyst	V _{N2} ^a (ml g ⁻¹)	V _{Hg} ^b (ml g ⁻¹)	A _p ^c (m ² g ⁻¹)	D _p ^d (nm)	Porosity ^e (%)
IO-TiO ₂ -155	0.09	1.4	36.6	153	80.1
IO-TiO ₂ -195	0.10	1.8	37.6	191	83.7
IO-TiO ₂ -285	0.13	2.7	39.3	274	89.5

^a Pore volume determined by BET method.

^b Total pore volume for pores.

^c Total pore area determined by Hg porosimetry.

^d The average pores diameter.

^e Determined by Hg porosimetry.

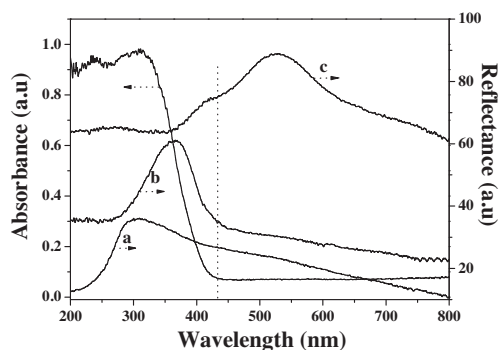


Fig. 4. The UV-vis absorbance/reflectance spectra of IO-TiO₂ catalysts with different pore sizes. (a) IO-TiO₂-155; (b) IO-TiO₂-195; (c) IO-TiO₂-285.

525 nm, respectively. At the edges of the photonic band gap (PBG), light travels with a strongly reduced group velocity (v_g) resulting in the creation of slow photons. At the 'red edge' of the PBG, the incident light is localized on the dielectric material. The 'red edge' of the PBG for IO-TiO₂-195 material is coupled to the electronic absorption edge of TiO₂ (~ 440 nm), which should in theory enhance light absorption by the semiconductor and should enhance the photocatalytic activity. The phenomenon may be ascribed to its slow photon effect of ordered macroporous structure and multiple scattering enable it to harvest light with much high efficiency. The IO-TiO₂ will be hereafter considered as one of the suitable support systems for the improving catalytic activity of CO₂ reduction with H₂O. Therefore, we chose the IO-TiO₂-195 material as a carrier in the following research.

3.3. The characterization of Au@CdS/IO-TiO₂-*n* catalysts

Fig. 5 shows the XRD patterns of IO-TiO₂, Au/IO-TiO₂ and Au@CdS/IO-TiO₂ catalysts. The diffraction peaks (2θ) at 25.3, 37.8,

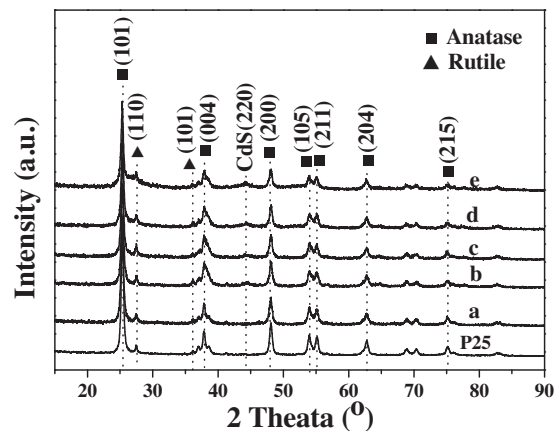


Fig. 5. XRD patterns of IO-TiO₂, Au/IO-TiO₂ and Au@CdS/IO-TiO₂ catalysts prepared by GBMR/P method. (a) IO-TiO₂; (b) Au/IO-TiO₂; (c) Au@CdS/IO-TiO₂-1; (d) Au@CdS/IO-TiO₂-2; (e) Au@CdS/IO-TiO₂-4.

48.0, 53.9, 55.1, 62.7 and 75.0° can be indexed to the (1 0 1), (0 0 4), (2 0 0), (1 0 5), (2 1 1), (2 0 4) and (2 1 5) crystal faces of IO-TiO₂ with a tetragonal anatase structure (PDF# 21-1272), respectively. And the weak diffraction peaks (2θ) at 27.4 and 36.1° can be indexed to the (110) and (101) crystal faces of IO-TiO₂ with a tetragonal rutile structure (PDF# 65-0191). It indicates the coexistence of the two crystal phases' structures for IO-TiO₂ support, which is similar to the phase structure of P25. After loading Au@CdS core-shell NPs, the extremely weak diffraction peaks (2θ) at 44.0° over Au@CdS/IO-TiO₂-4 catalysts can be observed, which is indexed to the (220) crystal faces of CdS with a cubic hawleyite structure (PDF#10-0454), and the characteristic diffraction peaks belonging to supported Au NPs were not detected. It indicates that the sizes of supported Au and CdS NPs on the surface of IO-TiO₂ support may be beyond the detection limit of XRD spectra (<4 nm). The average

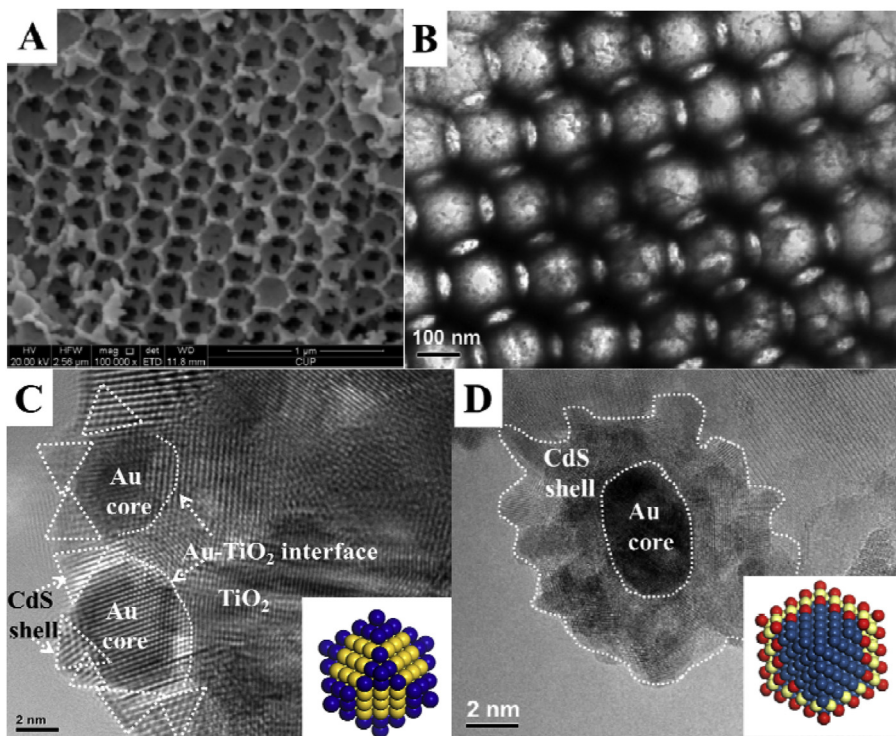


Fig. 6. SEM, TEM and HRTEM images of Au@CdS/IO-TiO₂ catalysts. The insets in C and D images correspond to the different thickness of CdS shell layer on the surface of Au core. A–C: Au@CdS/IO-TiO₂-1; D: Au@CdS/IO-TiO₂-4.

Table 2

The crystal parameters and average crystal sizes of IO-TiO₂, Au/IO-TiO₂ and Au@CdS/IO-TiO₂ catalysts.

Catalyst	<i>D</i> ^a of TiO ₂ (nm)	Au size ^b (nm)	<i>S</i> _{BET} ^c (m ² g ⁻¹)	Au content ^d (wt%)
IO-TiO ₂	19.6	–	56	–
Au/IO-TiO ₂	20.1	3.4	57	3.2
Au@CdS/IO-TiO ₂ -1	19.8	3.5	54	3.3
Au@CdS/IO-TiO ₂ -2	20.0	3.6	52	3.1
Au@CdS/IO-TiO ₂ -4	20.1	3.5	51	3.0

^a Determined by XRD using Scherrer equation with the intensity of the most prominent peak, (1 0 1).

^b Determined by HRTEM.

^c Surface area obtained by BET method.

^d Determined by ICP-AES.

crystalline size of IO-TiO₂ oxide determined by Scherrer equation is about 19.0 nm. No obvious change of its crystalline size is observed after Au and CdS NPs supported on IO-TiO₂.

Fig. 6 shows the SEM, TEM and HRTEM images of Au@CdS/IO-TiO₂-*n* catalysts synthesized via the GBMR/P method. In this catalyst system, the initial weight percent of Au to TiO₂ in the catalysts is always 4 wt%, and *n* is the theoretical molar ratio of CdS to Au. As shown in Fig. 6A, the macroporous structure of Au@CdS/IO-TiO₂-1 catalyst contains periodic voids with average diameter of 195 ± 10 nm and wall thickness of 30 ± 5 nm, which is similar to that of inverse opal IO-TiO₂ support. It indicates that the process of the CdS deposition via GBMR/P method cannot obviously affect the macroporous structure of IO-TiO₂ support. And the inverse opal structure with overlapped pores can be further observed by TEM images. As shown in Fig. 6C and D, it clearly shows the formation of the core-shell structural Au@CdS NPs. The thickness and morphology of the CdS nano-shell over Au NPs can be adjusted and controlled in the range of 0–3 nm. The sizes of Au@CdS core-shell NPs are in the range of 4–10 nm, and the mean diameters of Au core are 3.5 ± 1.0 nm and the results are shown in Table 2. With the increasing of Cd/Au molar ratio, the morphology of CdS nano-shell deposited on the surface of Au NPs changes from the isolated nano-islands (Fig. 6C) to the full cover layers (Fig. 6D), indicating that the thickness and morphology of CdS nano-shell can be adjusted and controlled by the feeding molar ratio of Cd/Au. In addition, the BET surface areas of as-prepared catalysts are also summarized in Table 2. The BET surface area of IO-TiO₂ oxide support is 56 m² g⁻¹. With increasing of CdS/Au ratio, the BET surface area slightly decreases. In a word, the CdS shell is coated selectively on the surface of Au NPs by the GBMR/P method, and the CdS(shell)-Au(core)-TiO₂(support) nanojunction system was constructed successfully, which ensures the efficient photogenerated electron transfer and the subsequent photocatalysis.

In order to investigate the periodic effect and electronic effect of Au@CdS/IO-TiO₂ catalysts, UV-vis diffuse reflectance spectroscopy (DRS) studies were performed and the results are shown in Fig. 7A. After supporting Au, CdS and Au@CdS NPs, the catalysts show spectral response in a broad visible region (400–800 nm) owing to the photosensitizing effect of Au and CdS. It is worthy to note that Au@CdS/IO-TiO₂ catalysts exhibit a much stronger absorption in visible-light regions (450–650 nm) than that of IO-TiO₂, the enhanced light-trapping effect is attributed to the surface plasmon resonance (SPR) of supported Au NPs. With increasing the molar ratio of CdS to Au, the relative intensity of absorption peak centered at 550 nm decreases remarkably, indicating that the surface of Au NPs are covered by the CdS nanolayers. It is an indirect proof for the formation of Au@CdS core-shell NPs on the surface of IO-TiO₂. The band energy gap of above samples could be calculated by using $(\alpha h\nu)^n = A(h\nu - E_g)$, where α is the absorption coefficient, *A* is the parameter that is related to the effective masses associated with the valence and conduction bands, *n* is 1/2 for a direct transi-

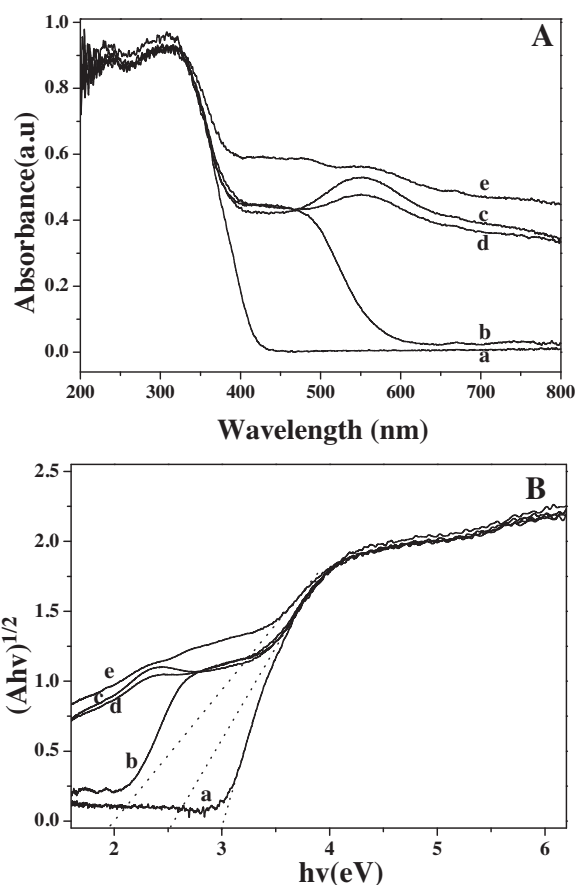


Fig. 7. UV-vis DRS (A) and Kubelka-Munk transformed reflectance spectra to estimate optical absorption band gap (B) of the typical catalysts. (a) IO-TiO₂-195; (b) CdS/TiO₂; (c) Au/IO-TiO₂; (d) Au@CdS/IO-TiO₂-1; (e) Au@CdS/IO-TiO₂-4.

tion, $h\nu$ is the absorption energy, and E_g is the band gap energy [45]. Plotting $(\alpha h\nu)^{1/2}$ versus $h\nu$ based on the spectral response in Fig. 7A gives the extrapolated intercept corresponding to the E_g value, and the results are shown in Fig. 7B. The E_g values of CdS/IO-TiO₂ catalyst (2.40 eV) and Au/IO-TiO₂ catalyst (2.50 eV) are much smaller than that of IO-TiO₂ catalyst (3.05 eV). It indicates that the addition of CdS and Au NPs resulted in the additional absorption band in the visible region. With the increasing of Cd/Au molar ratios, the optical band gap energies display red-shift in comparison with those of Au/TiO₂ and CdS/TiO₂. The results indicate that the enhanced ability to absorb visible-light of Au@CdS/IO-TiO₂ catalysts makes them as a promising photocatalyst for solar-driven applications.

Photoluminescence (PL) spectra are usually used to explore the efficiency of the charge carrier trapping, migration, and transfer, and it is quite helpful to understand the fate of electron-hole pairs in semiconductor particles as PL emission arises from the recombination of free carriers. The intensity of the PL emission spectra depends on the recombination of excited electrons and holes. The lower the PL emission intensity is, the lower the recombination property of the samples is. Fig. 8 shows the PL spectra of IO-TiO₂, CdS/IO-TiO₂, Au/IO-TiO₂ and Au@CdS/IO-TiO₂ catalysts. The excitation wavelength was set at 300 nm. It can be observed that IO-TiO₂ catalyst shows the strong emission peaks during 390–430 nm and 440–500 nm at ambient temperature, which might be attributed to the emission of the bandgap transition of 2.85 eV and that of the charge transfer transition of oxygen vacancy trapped electrons, respectively [29]. After introduction of Au NPs and CdS nanolayers, their PL emission intensities obviously decrease, indicating that the tri-coupling of TiO₂, Au and

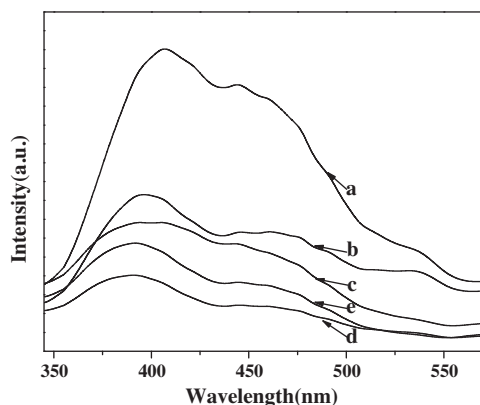


Fig. 8. Photoluminescence (PL, $\lambda_{\text{ex}} = 300$ nm) spectra of the typical catalysts. (a) IO-TiO₂-195; (b) CdS/IO-TiO₂; (c) Au/IO-TiO₂; d. Au@CdS/IO-TiO₂-1; (e) Au@CdS/IO-TiO₂-4.

CdS in the heterostructures effectively diminished the recombination of photogenerated electron-hole pairs, which is beneficial to improving the photocatalytic activity for CO₂ reduction. Among the catalysts, Au@CdS/IO-TiO₂-1 catalyst shows the lowest recombination efficiency of photoinduced electron-hole pairs. With the increasing of CdS thickness, Au@CdS/IO-TiO₂-4 catalyst shows the higher recombination efficiency of photoinduced electron-hole pairs than Au@CdS/IO-TiO₂-1 catalyst due to the weakening role of CdS(shell)-Au(core)-TiO₂ (support) nanojunction for the separation of photogenerated electrons and holes. Therefore, the suitable ratio of Cd/Au can optimize the recombination efficiency of photo-generated electron-hole pairs.

It is acknowledged that the photocurrent observed under illumination reflects the number of charge carriers produced by the incident light. To further illustrate the function of the Au and CdS cocatalyst for promoting electron transfer in Au@CdS/IO-TiO₂ photocatalytic system, we investigated the photocurrent generation behavior of the system under light irradiation, and the photocurrent action spectra are showed in Fig. 9. For comparison, the experimental results of IO-TiO₂ and Au/IO-TiO₂ catalysts are also included. It is noted that, after the introduction of Au nanoparticles and CdS, the photocurrent generation is enhanced remarkably, and the photocurrent intensity of Au@CdS/IO-TiO₂-1 catalyst is highest. It is well-known that the diffusion of the photoinduced electrons to the back contact and the acceptance of the photo-generated holes by the hole acceptor are the main reasons for

photocurrent generation. With the increasing of CdS loading ($n > 1$), the role of CdS(shell)-Au(core)-TiO₂(support) nanojunction for the separation of photogenerated electrons and holes is weakened remarkably, and the recombination efficiency of photoinduced electron-hole pairs on the surface of CdS nanolayer increases. Therefore, the enhanced photocurrent generation of the system reflected effective transport of light-induced charge carriers, which is also consistent well with the results of the PL measurements. All the observations highlighted the outstanding performance of the catalysts with IO-TiO₂-supported Au@CdS core-shell NPs for enhancing charge transfers in the photochemical CO₂ reduction system.

3.4. Photocatalytic activity for CO₂ reduction under simulated solar irradiation

The photocatalytic activities of the as-prepared catalysts for CO₂ reduction with H₂O were measured in a gas-closed circulation system under simulated light irradiation (wavelength: 32–780 nm). Commercial P25 was selected as the reference catalyst in photoreduction of CO₂. A series of background tests were performed: in the absence of photocatalysts, or light irradiation, or CO₂ gas, the hydrocarbon products had not been detected. In addition, the analysis result of ¹³C isotopic tracing via GC-MS for the products of photocatalytic ¹³CO₂ reduction over Au@CdS/IO-TiO₂ catalyst after 20 h irradiation is shown in Fig. S6. It indicates that the C element in the product of CO and CH₄ comes from CO₂ reactant. Therefore, we assert that the conversion products were derived from CO₂ in the feed gas. According to the test results, we can learn that the process of CO₂ reduction requires both photocatalysts and light irradiation.

The photocatalytic reduction of CO₂ with H₂O provided CO and CH₄ as two main carbon products, and the formation of H₂ and O₂ was also observed at the same time. As shown in Table 3, IO-TiO₂-195 catalyst shows higher catalytic activity than those of commercial P25, IO-TiO₂-155 and IO-TiO₂-285 catalysts, indicating that the slow photon effect of inverse opal structure can obviously improve the light harvesting efficiency. The loading of CdS or deposition of Au onto IO-TiO₂ can promote the formation of CO and CH₄ (H₂), respectively. Considering that the reduction of H₂O to H₂ is a competitive reaction with the reduction of CO₂ to CO and CH₄ [31], we have evaluated the selectivity for CO₂ reduction on an electron basis. It becomes clear that the Au co-catalyst decreases the selectivity for CO₂ reduction, whereas the selectivity increases from 60.4 to 73.3% by loading CdS onto TiO₂. The Au@CdS/IO-TiO₂ catalysts exhibited a significantly enhanced activity for the formation

Table 3
The formation rates of H₂, CO and CH₄, the selectivities for CO₂ reduction, the selectivities for CO and CH₄ productions, and the electron balance evaluation for photocatalytic conversion of CO₂ with H₂O over Au/IO-TiO₂, Au@CdS/IO-TiO₂ and CdS/IO-TiO₂ catalysts.^a

Sample	Formation rate [$\mu\text{mol g}^{-1} \text{h}^{-1}$] ^a				S _{CO2} (%) ^b	S _{CO} (%) ^c	S _{CH4} (%) ^c	Electron balance evaluation ^d
	H ₂	O ₂	CO	CH ₄				
P25	3.8	N.d. ^e	1.8	1.3	64.8	58.1	41.9	N.d. ^e
IO-TiO ₂ -155	3.9	N.d.	2.5	1.4	67.5	64.1	35.9	N.d.
IO-TiO ₂ -195	6.1	N.d.	2.9	1.6	60.4	64.4	35.6	N.d.
IO-TiO ₂ -285	5.2	N.d.	2.7	1.5	62.6	64.3	35.7	N.d.
CdS/IO-TiO ₂	4.3	N.d.	4.6	1.8	73.3	71.9	28.1	N.d.
Au/IO-TiO ₂	65.6	55.8	0.2	5.1	23.9	3.8	96.2	1.29
Au@CdS/IO-TiO ₂ -0.5	30.7	66.1	0.8	18.5	70.9	4.1	95.9	1.25
Au@CdS/IO-TiO ₂ -1	18.2	109.5	0.6	41.6	90.2	1.4	98.6	1.18
Au@CdS/IO-TiO ₂ -2	16.6	83.6	1.2	26.2	86.5	4.4	95.6	1.36
Au@CdS/IO-TiO ₂ -4	12.5	52.1	3.1	15.8	84.1	16.4	83.6	1.32
Au@CdS/P25-1	24.6	53.1	0.7	15.6	71.9	4.3	95.7	1.21

^a Reaction conditions: photocatalyst, 0.02 g; CO₂ pressure, 0.1 MPa; H₂O, 1.0 mL; light source, 320–780 nm; irradiation time, 2 h; reaction temperature, 20 °C.

^b The selectivity for CO₂ reduction was evaluated on an electron basis, equation: Selectivity (%) = $[2n(\text{CO}) + 8n(\text{CH}_4)] / [2n(\text{CO}) + 8n(\text{CH}_4) + 2n(\text{H}_2)] \times 100\%$.

^c Based on the ratio of [CO] or [CH₄] amounts to sum ([CO] + [CH₄]) amounts.

^d The electron balance was evaluated by the ratio of $[4n(\text{O}_2)]$ amounts to $[2n(\text{CO}) + 8n(\text{CH}_4) + 2n(\text{H}_2)]$ amounts.

^e Not determined.

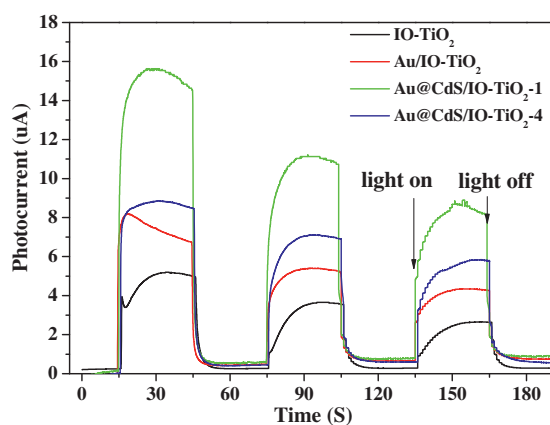


Fig. 9. Transient photocurrent response of CO₂ reduction system included different components under visible light irradiations (> 320 nm).

of CH₄. Among the as-prepared catalysts, Au@CdS/IO-TiO₂-1 catalyst shows the highest formation rate of CH₄ ($41.6 \mu\text{mol g}^{-1} \text{h}^{-1}$) and the low formation rate of CO ($0.6 \mu\text{mol g}^{-1} \text{h}^{-1}$), its selectivity to CH₄ production by CO₂ reduction is 98.6%. The formation rate of CH₄ over Au@CdS/IO-TiO₂-1 catalyst is about 26 times higher than that of IO-TiO₂-195 alone, and is 23 and 8 times higher than those of CdS/IO-TiO₂ and Au/IO-TiO₂ catalysts, respectively. And the catalytic activity of Au@CdS/IO-TiO₂-1 catalyst is remarkably higher than that of Au@CdS/P25-1 catalyst in Table 3, which is attributed to the structure effect of the inverse opal TiO₂ for improving the light-absorption. With the increasing of CdS loading amount, the formation rate of CH₄ decreases and the formation rate of CO increases, indicating that the thickness of CdS shell has a significant impact on the catalytic activity and selectivity for CO₂ reduction. The excess deposition of CdS on Au core suppressed the reduction of H₂O to H₂ and preferentially accelerated the reduction of CO₂ to CO due to the weakening role of CdS(shell)-Au(core)-TiO₂ (support) nanojunction for the separation of photogenerated electrons and holes. Moreover, we further confirmed the formation rate of O₂ over the as-prepared catalysts. Among all the catalysts, Au@CdS/IO-TiO₂-1 catalyst shows the highest formation rate of O₂ ($109.5 \mu\text{mol g}^{-1} \text{h}^{-1}$), which is higher than the stoichiometric rate according to the calculation of other production ($92.6 \mu\text{mol g}^{-1} \text{h}^{-1}$) [31]. And the electron balance was evaluated by the ratio of $[4n(\text{O}_2)]$ amounts to $[2n(\text{CO}) + 8n(\text{CH}_4) + 2n(\text{H}_2)]$ amounts and the results are shown in Table 3. The values of electron balance evaluation are larger than 1.00, indicating that the number of used photogenerated holes is more than that of consumed electrons. It may be attributed to the formation of other undetected hydrocarbon. Therefore, it is concluded that the moderate thickness of CdS shell on the surface of Au core is favorable for CO₂ reduction and can enhance the formation rate of CH₄.

We further investigated the stability of photocatalytic activity for the formation rate of H₂, CH₄ and CO over Au@CdS/IO-TiO₂-1 catalyst via test cycles, and the results are shown in Fig. 10. The Au@CdS/IO-TiO₂-1 catalyst maintains its high catalytic activities for the photocatalytic reduction of CO₂ with H₂O in five test cycles under the same reaction condition, i.e., the fifth cycle values for the formation rate of H₂, CH₄ and CO are 17.8, 40.8 and $0.8 \mu\text{mol g}^{-1} \text{h}^{-1}$, respectively, which have not obviously changed in comparison with the first cycle values (Table 1). And based on the results of SEM (Fig. S7), TEM (Fig. S8), and XPS (Fig. S9), it is proved that, after the five test cycles of photocatalytic reduction of CO₂ with H₂O, the macropore structure and the electronic properties of surface elements over Au@CdS/IO-TiO₂-1 catalyst have not obviously changed in comparison with the fresh catalyst. It indicates that the Au@CdS/IO-TiO₂ catalysts have the good stability of

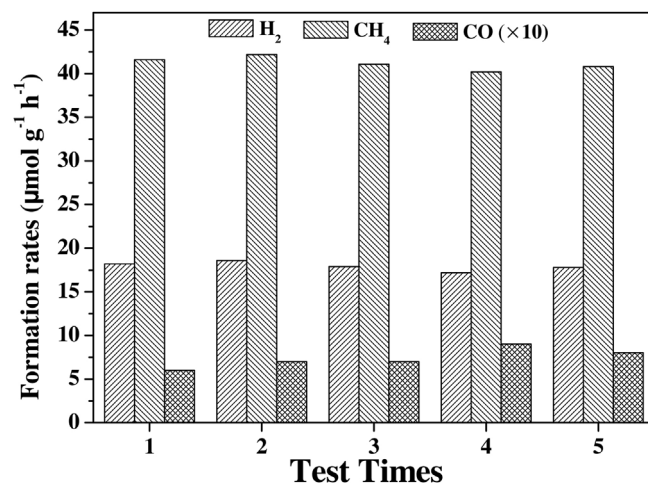


Fig. 10. Stability study on the formation rate of H₂, CH₄ and CO over Au@CdS/IO-TiO₂-1 catalyst for five test cycles. In order to clearly show the CO formation rate, the values are magnified to 10 times.

structure and photocatalytic activity for CO₂ reduction with H₂O under the simulated solar irradiation.

4. Discussions

It is well-known that the design of photocatalysts for CO₂ reduction to CO and CH₄ must be meet the energy band theory, which is based on the relative positions of conductance band (CB), valance band (VB) and oxidation potentials. In general, photogenerated electrons can be consumed effectively, if the reduction potential of the reaction is lower than the conductance band potential of these semiconductor. The reactions can occur during photocatalytic CO₂ with H₂O to produce CO and CH₄ in terms of thermodynamic reduction potentials versus normal hydrogen electrode (NHE). For example, the conduction band potentials (E_{CB}) of TiO₂ and CdS are -0.56 and -1.0 V (vs. NHE at pH 7), respectively [46]. And the reduction potential of $E^{\theta}(\text{CO}_2/\text{CO}) = -0.53$ V is lower than the E_{CB} of TiO₂ and CdS [47]. Since the CB flat band potential is more negative than the CO₂/CO reduction potential, the reduction reaction is theoretically feasible. For CO₂ reduction to CH₄, the lower reduction potential difference ($E^{\theta}(\text{CO}_2/\text{CH}_4) = -0.24$ V) also drive the reaction. Although the reduction potential values of $E^{\theta}(\text{CO}_2/\text{CH}_4)$ is less negative than that of $E^{\theta}(\text{CO}_2/\text{CO})$, eight electrons are required to produce CH₄ compared with only two for CO production. Thus, it is significant to observe that the formation rates of CO and CH₄ in the gaseous product mixtures change with the nanostructure and composition of as-prepared catalysts.

For the reaction of photocatalytic CO₂ reduction with H₂O vapors under the simulated solar irradiation, CO, CH₄, H₂ and O₂ were produced by CO₂ reduction and H₂O oxidation. The first step in photocatalysis reaction should be the production of electron-hole pairs when optical wave is absorbed by the surface of photocatalysts. The electrons (e^-) transferred from the conduction band of photocatalysts for the activation of CO₂. The reduction proceeds through a series of elementary steps which involve the transfer of an electron, a proton, or hydrogen radical (H^{\bullet}), as well as breaking C–O bonds and creating new C–H bonds. On the other hand, holes (h^+) are used to oxidize H₂O and formation of surface-bound hydrogen ions (H^+) and hydroxyl radical (OH^{\bullet}) which is further oxidized to the production of O₂ and H^+ . Some of the intermediates are radical species, whose recombination at different stages partially accounts for the number of possible pathways and final products. The exact order and mechanistic details of each subsequent step have not been fully elucidated, but three full path-

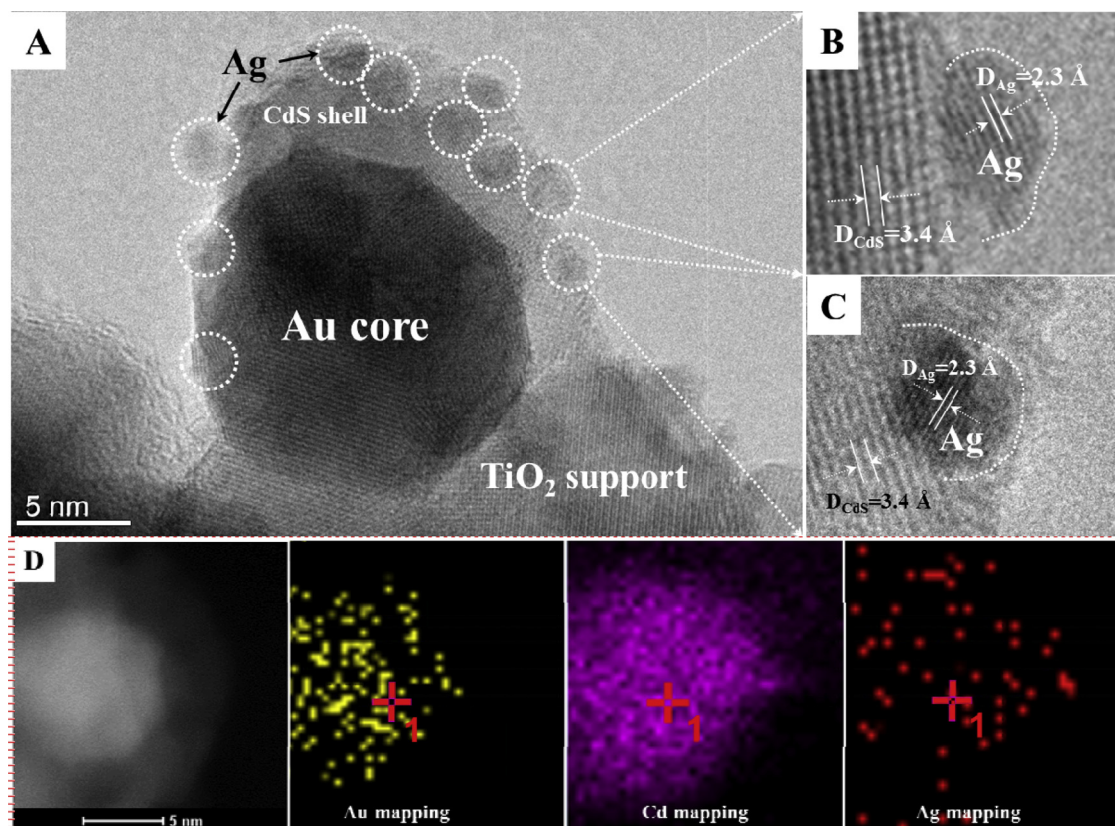


Fig. 11. HRTEM images (A–C) and HAADF-STEM-EDS elemental mapping (D) of Ag/Au@CdS/IO-TiO₂ catalyst obtained by Ag photodeposition on the surface of Au@CdS/IO-TiO₂-1 catalyst with UV–vis light (320–780 nm) irradiation for 30 min. B and C images are the magnified images of Ag NP in A image. In D image, the yellow, pink and red color indicates Au, Cd and Ag elementals determined by EDS analysis, respectively. (For interpretation of the references to colour in this figure legend, the reader is referred to the web version of this article).

ways for the conversion of CO₂ to CH₄ have been proposed in the literature. In the following discussion, they are referred to as (1) the formaldehyde pathway, (2) the carbene pathway, and (3) the glyoxal pathway on account of their unique intermediate [48]. For co-catalysts with coupling semiconductors with metal NPs, they have been shown to be beneficial for the performance of photocatalysts because of, among other factors, improved charge separation, facilitated CO₂ activation, and the provision of catalytic active sites for the reduction process. In a typical realization of this concept, the often nanostructured semiconductor is surface-decorated with metal or metal oxide NPs. This architecture is utilized in almost all of the most efficient photocatalytic systems. It is a convenient setup which allows the catalytic process to be isolated from the light-harvesting and charge-separation functions of the photocatalyst.

Based on the results of the formation rates of H₂, CO and CH₄ (Table 3) and the nanostructure of Au@CdS/IO-TiO₂ catalysts (Fig. 6), the enhanced photocatalytic activity for CO₂ reduction can be ascribed to their unique structure with a variety of favorable properties. On the one hand, the slow photon enhancement of inverse opal structure plays an important role for improving photocatalytic activity. On the other hand, the introduction of Au@CdS core-shell NPs in CdS-Au-TiO₂ nanojunction can effectively extend the spectral response from UV to visible area owing to the CdS-photosensitization and improve separation of photogenerated charge carriers [32]. According to the result of UV–vis DRS in Fig. 7, TiO₂ support can absorb the light wave with the wavelength of 320–400 nm in this photocatalytic reaction, CdS can absorb the light wave with the wavelength of >320 nm, and supported Au NPs can further improve the absorption for visible light due to the sur-

face plasmon resonance. Therefore, the Au@CdS/IO-TiO₂ catalysts show the high absorption efficiency for the light irradiation due to the synergistic effect of Au@CdS core-shell NPs and inverse opal structural support.

The Au@CdS/IO-TiO₂ catalysts can be divided into three systems for mechanism research: isolated photochemical system 1 (Au/TiO₂), isolated photochemical system 2 (CdS/Au) and the electron-transfer system 3 (Au). After the absorption of photons, both TiO₂ and CdS are excited to produce electron-hole pairs. For the system 1, the generated electrons in the conduction band (CB) of TiO₂ flow into Au, i.e., electron transfers from TiO₂ to Au. It is attributed to the different Fermi levels between Au and the CB-edge of TiO₂ and the formation of Schottky barrier at the Au and TiO₂ interface. For the system 2, the VB-holes of CdS could be recombination with electrons derived from the Au sensor because of the formation of the inner electric field with abundant electron over Au NPs and the surface plasmon resonance of Au NPs, i.e., the electron transfer from Au to CdS. And the CB-electrons of CdS would be used for CO₂ reduction rather than transferred to Au because of the increase in their surface population in the Au@CdS core-shell structure. Thus, the vectorial electron transfer of TiO₂ → Au → CdS should occur as a result of excitation of both TiO₂ and CdS under the conditions of CO₂ reduction. In other words, the Au@CdS/IO-TiO₂ catalyst is an all-solid-state Z-scheme system with CdS-Au-TiO₂ nanojunction [32]. Combined the results of PL spectra (Fig. 8), the photocurrent action spectra (Fig. 9) and catalytic activity (Table 3), the Au@CdS/IO-TiO₂-1 catalyst shows the lowest recombination efficiency of photoinduced electron-hole pairs and the highest catalytic activity for CO₂ reduction, indicating that the all-solid-state CdS-Au-TiO₂ Z-scheme system with optimized pore size and molar

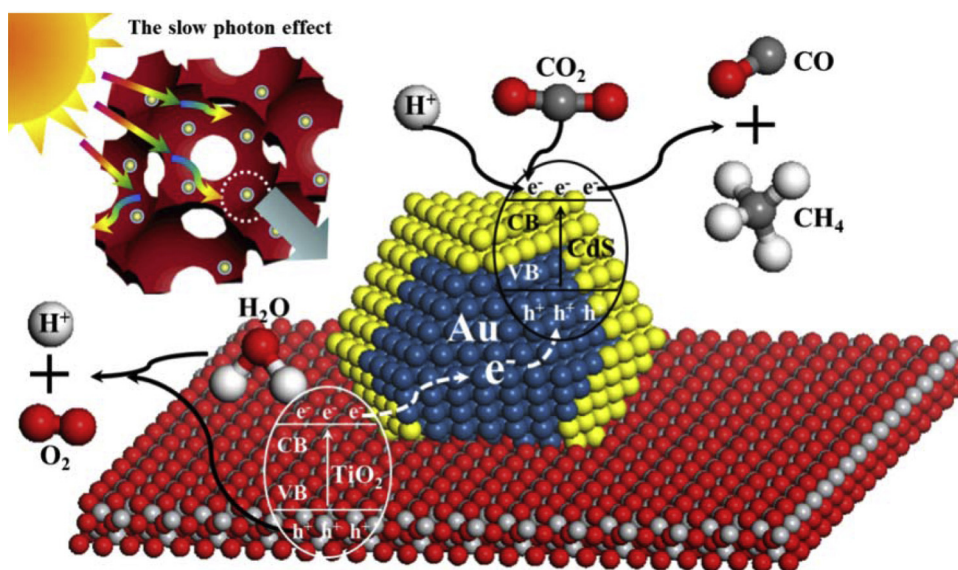


Fig. 12. Mechanism for the photoreduction of CO_2 with H_2O over Au@CdS/IO-TiO_2 catalysts.

ratio of Cd/Au is conducive to diminishing the recombination of photogenerated electron-hole pairs and improving the photocatalytic activity for CO_2 reduction.

In order to specify the vectorial electron transfer of $\text{TiO}_2 \rightarrow \text{Au} \rightarrow \text{CdS}$ and the reduction sites of Au@CdS/IO-TiO_2 , the experiment of Ag photodeposition was carried out by irradiation with same light source of CO_2 reduction test for 30 min, and the results are shown in Fig. 11. If the electron transfer from CdS to TiO_2 rapidly takes place through their contact with Au NPs, Ag NPs should be deposited on TiO_2 . However, HRTEM images show that Ag nanoparticles are deposited on the surface of CdS shell layer (Fig. 11A) and there is the clearly contrast between Ag nanoparticles and CdS nanolayer (Fig. 11B and C). It indicates that Ag nanoparticles are deposited almost selectively on the surface of CdS shell layer and formation of the Ag photodeposited on Au@CdS/IO-TiO_2 ($\text{Ag}/\text{Au@CdS/IO-TiO}_2$). And the result is further demonstrated by the HAADF-STEM-EDS elemental mapping of $\text{Ag}/\text{Au@CdS/IO-TiO}_2$ catalyst in Fig. 11D, which the yellow, pink and red color indicates Au, Cd and Ag elements determined by EDS analysis, respectively. Therefore, it is deduced that CdS acts as the reduction sites of Au@CdS/IO-TiO_2 catalysts, and the back electron transfer from CdS to TiO_2 is a minor path, which strongly supports the vectorial electron transfer in the all-solid-state CdS-Au- TiO_2 Z-scheme system. The Z-scheme system simultaneously generates VB-holes (TiO_2) with a strong oxidation power and CB-electrons (CdS) with a strong reduction power, which explains the high formation rates of CH_4 from CO_2 reduction. These results can also be interpreted as that the electron supply from TiO_2 to CdS via Au in the Z-scheme system restricts the self-decomposition of CdS.

According to the discussion above, the mechanism for the photoreduction of CO_2 with H_2O over Au@CdS/IO-TiO_2 catalysts is proposed and shown in Fig. 12. Firstly, the slow photon effect of inverse opal structure can improve the light-harvesting efficiency, which is an important factor for enhancing photocatalytic performance for CO_2 reduction. Secondly, the vectorial electron transfer of $\text{TiO}_2 \rightarrow \text{Au} \rightarrow \text{CdS}$ over the all-solid-state Z-scheme system benefits the separation of photogenerated electrons and holes, which can increase the formation rates and selectivity of CH_4 for CO_2 reduction. Under the simulated solar irradiation, the generated CB-electrons of TiO_2 flow into Au NPs, and the electron further transfers to CdS shell and quenches with the VB-holes of CdS, which achieve the high separation efficiency of photogenerated electron-

hole pairs in CdS-Au- TiO_2 nanojunction system due to the vectorial electron transfer. Finally, the VB-holes of TiO_2 support can oxidize H_2O to O_2 and H^+ , and the abundant CB-electrons of CdS shell would be used for CO_2 reduction and preferentially generate CH_4 . Therefore, Au@CdS/IO-TiO_2 catalysts, which takes both advantages of the high light-harvesting efficiency by 3DOM supports and the high separation of photogenerated electrons and holes by the all-solid-state Z-scheme system with CdS-Au- TiO_2 nanojunction, show super photocatalytic performance for CO_2 reduction into CH_4 under the simulated solar irradiation.

5. Conclusions

In summary, we demonstrated a strategy for preparing the photocatalysts that consists of the core-shell-structured Au@CdS NPs uniformly dispersed on IO-TiO_2 via the GBMR/P method. The core-shell structural Au@CdS NPs with adjustable thickness of the CdS shell are dispersed on the inner walls of uniform macropores. The slow photon effect of inverse opal structural TiO_2 with moderate pore sizes can improve the light-harvesting efficiency. The vectorial electron transfer ($\text{TiO}_2 \rightarrow \text{Au} \rightarrow \text{CdS}$) of all-solid-state Z-scheme system with CdS(shell)-Au(core)- TiO_2 (support) nanojunction is favorable for the separation of photogenerated electrons and holes. The Au@CdS/IO-TiO_2 catalysts, which takes both advantages of the high light-harvesting efficiency and the high separation of photogenerated electrons-holes, exhibited super photocatalytic performance for CO_2 reduction with H_2O . Our design and versatile synthetic approach can potentially be extended to other nanoparticle cores with different compositions, sizes and shapes and to other shell compositions on the surface of 3D photonic crystal support. The fabrication of all-solid-state Z-scheme system on inverse opal oxides surface is expected to throw new light on the design of highly efficient photocatalyst for CO_2 reduction to hydrocarbon.

Acknowledgements

We acknowledge the financial support from the National Natural Science Foundation of China (No. 21177160 and 21303263), Beijing Nova Program (No. Z141109001814072), Specialized Research Fund for the Doctoral Program of Higher Education of China (No. 20130007120011) and Science Foundation of China Uni-

versity of Petroleum, Beijing (QZDX-2011-02, No. 2462013YJRC13 and 2462013BJRC003)

Appendix A. Supplementary data

Supplementary data associated with this article can be found, in the online version, at <http://dx.doi.org/10.1016/j.apcatb.2015.05.041>

References

- [1] F. Zuo, L. Wang, T. Wu, Z. Zhang, D. Borchardt, P. Feng, *J. Am. Chem. Soc.* 132 (2010) 11856–11857.
- [2] E.V. Kondratenko, G. Mul, J. Baltrusaitis, G.O. Larrazábal, J. Perez-Ramirez, *Energy Environ. Sci.* 6 (2013) 3112–3135.
- [3] T. Inoue, A. Fujishima, S. Konishi, K. Honda, *Nature* 277 (1979) 637–638.
- [4] M. Tahir, N.S. Amin, *Appl. Catal. B* 162 (2015) 98–109.
- [5] S. Sato, T. Morikawa, T. Kajino, O. Ishitani, *Angew. Chem. Int. Ed.* 52 (2013) 988–992.
- [6] A. Dhakshinamoorthy, S. Navalon, A. Corma, H. Garcia, *Energy Environ. Sci.* 5 (2012) 9217–9233.
- [7] Y. Wei, J. Jiao, Z. Zhao, W. Zhong, J. Li, J. Liu, G. Jiang, A. Duan, *J. Mater. Chem. A* 3 (2015) 11074–11085.
- [8] S. Xie, Y. Wang, Q. Zhang, W. Fan, W. Deng, Y. Wang, *Chem. Comm.* 49 (2013) 2451–2453.
- [9] S. Yan, S.X. Ouyang, J. Gao, M. Yang, J. Feng, X. Fan, L. Wan, Z. Li, J. Ye, Y. Zhou, Z. Zou, *Angew. Chem. Int. Ed.* 49 (2010) 6400–6404.
- [10] Y. Ma, X. Wang, Y. Jia, X. Chen, H. Han, C. Li, *Chem. Rev.* 114 (2014) 9987–10043.
- [11] V.P. Indrakanti, J.D. Kubickib, H.H. Schobert, *Energy Environ. Sci.* 2 (2009) 745–748.
- [12] K. Kočí, L. Obalová, L. Matějová, D. Plachá, Z. Lacný, J. Jirkovský, O. Šolcová, *Appl. Catal. B* 89 (2009) 494–502.
- [13] Q. Zhang, T. Gao, J.M. Andino, Y. Li, *Appl. Catal. B* 123–124 (2012) 257–264.
- [14] S.N. Habisreutinger, L. Schmidt-Mende, J.K. Stolarczyk, *Angew. Chem. Int. Ed.* 52 (2013) 7372–7408.
- [15] T. Kamegawa, N. Suzuki, H. Yamashita, *Energy Environ. Sci.* 4 (2011) 1411–1416.
- [16] K. Ji, H. Dai, J. Deng, H. Zang, H. Arandiyán, S. Xie, H. Yang, *Appl. Catal. B* 168–169 (2015) 274–282.
- [17] J. Liu, G. Liu, M.Z. Li, W.Z. Shen, Z. Liu, J. Wang, J. Zhao, L. Jiang, Y. Song, *Energy Environ. Sci.* 3 (2010) 1503–1506.
- [18] P.G. O'Brien, N.P. Kherani, S. Zukotynski, G.A. Ozin, E. Vekris, N. Tetreault, A. Chutinan, S. John, A. Mihi, H. Miguez, *Adv. Mater.* 19 (2007) 4177–4182.
- [19] M. Wu, Y. Li, Z. Deng, B.L. Su, *ChemSusChem* 4 (2011) 1481–1488.
- [20] J.L.L. Chen, G.A. Ozin, *J. Mater. Chem.* 19 (2009) 2675–2678.
- [21] S. Wang, X. Wang, *Appl. Catal. B* 162 (2015) 494–500.
- [22] J. Chen, G. Li, Y. Huang, H. Zhang, H. Zhao, T. An, *Appl. Catal. B* 123 (2012) 69–77.
- [23] J. Jiao, Y. Wei, Z. Zhao, J. Liu, J. Li, A. Duan, G. Jiang, *Ind. Eng. Chem. Res.* 53 (2014) 17345–17354.
- [24] H.G. Yang, C.H. Sun, S.Z. Qiao, J. Zou, G. Liu, S.C. Smith, H.M. Cheng, G.Q. Lu, *Nature* 453 (2008) 638–641.
- [25] J. Guo, S. Ouyang, P. Li, Y. Zhang, T. Kako, J. Ye, *Appl. Catal. B* 134–135 (2013) 286–292.
- [26] J. Yang, D. Wang, H. Han, C. Li, *Acc. Chem. Res.* 46 (2013) 1900.
- [27] S. Watanabe, X. Ma, C. Song, *J. Phys. Chem. C* 115 (2009) 14249.
- [28] Y. Xie, G. Ali, S.H. Yoo, S.O. Cho, *ACS Appl. Mater. Interfaces* 2 (2010) 2910.
- [29] J. Tian, Y. Sang, Z. Zhao, W. Zhou, D. Wang, X. Kang, H. Liu, J. Wang, S. Chen, H. Cai, H. Huang, *Small* 9 (2013) 3864–3872.
- [30] X. Chen, X. Wang, X. Fu, *Energy Environ. Sci.* 2 (2009) 872.
- [31] Q. Zhai, S. Xie, W. Fan, Q. Zhang, Y. Wang, W. Deng, Y. Wang, *Angew. Chem. Int. Ed.* 52 (2013) 5776–5779.
- [32] H. Tada, T. Mitsui, T. Kiyonaga, T. Akita, K. Tanaka, *Nat. Mater.* 5 (2006) 782–786.
- [33] D. Chen, K. Wang, W. Hong, R. Zong, W. Yao, Y. Zhu, *Appl. Catal. B* 166–167 (2015) 366–373.
- [34] M. Zhang, X. Wang, *Energy Environ. Sci.* 7 (2014) 1902–1906.
- [35] L. Wang, J. Ge, A. Wang, M. Deng, X. Wang, S. Bai, R. Li, J. Jiang, Q. Zhang, Y. Luo, Y. Xiong, *Angew. Chem. Int. Ed.* 53 (2014) 5107–5111.
- [36] F. Wen, C. Li, *Acc. Chem. Res.* 46 (2013) 2355–2364.
- [37] Y. Wei, J. Liu, Z. Zhao, A. Duan, G. Jiang, C. Xu, J. Gao, H. He, X. Wang, *Energy Environ. Sci.* 4 (2011) 2959–2970.
- [38] Y. Wei, Z. Zhao, T. Li, J. Liu, A. Duan, G. Jiang, *Appl. Catal. B* 146 (2014) 57–70.
- [39] Y. Wei, Z. Zhao, J. Liu, S. Liu, C. Xu, A. Duan, G. Jiang, *J. Catal.* 317 (2014) 62–74.
- [40] Y. Wei, Z. Zhao, X. Yu, B. Jin, J. Liu, C. Xu, A. Duan, G. Jiang, S. Ma, *Catal. Sci. Technol.* 3 (2013) 2958–2970.
- [41] N. Zheng, G.D. Stucky, *J. Am. Chem. Soc.* 128 (2006) 14278–14280.
- [42] K.K.R. Datta, B.V.S. Reddy, K. Ariga, A. Vinu, *Angew. Chem. Int. Ed.* 49 (2010) 5961–5965.
- [43] Y. Wei, J. Liu, Z. Zhao, Y. Chen, C. Xu, A. Duan, G. Jiang, H. He, *Angew. Chem. Int. Ed.* 50 (2011) 2326–2329.
- [44] J.C. Love, L.A. Estroff, J.K. Kriebel, R.G. Nuzzo, G.M. Whitesides, *Chem. Rev.* 105 (2005) 1103–1170.
- [45] M. Yoon, M. Seo, C. Jeong, J.H. Kang, K.S. Jeon, *Chem. Mater.* 17 (2005) 6069–6079.
- [46] S. Sakthivel, M.C. Hidalgo, D.W. Bahnemann, S.U. Geissen, V. Murugesan, A. Vogelpohl, *Appl. Catal. B* 63 (2006) 31–40.
- [47] E.E. Benson, C.P. Kubiak, A.J. Sathrum, J.M. Smieja, *Chem. Soc. Rev.* 38 (2009) 89–99.
- [48] S.N. Habisreutinger, L. Schmidt-Mende, J.K. Stolarczyk, *Angew. Chem. Int. Ed.* 52 (2013) 7372–7408.